

Article

Superficial Modification of the Mg–Zn Biomaterials via Ion Nitriding for Biomedical Applications

Sergio Gonzaga ^{1,*}, Arturo Molina ², Rene Guardian ², Horacio Martínez ¹, Edna Vázquez-Vélez ¹
and Eduardo Lira-Díaz ^{3,4}

- ¹ Instituto de Ciencias Físicas, Universidad Nacional Autónoma de México, Av. Universidad 1000, Col. Chamilpa, Cuernavaca 62210, Mexico; hm@icf.unam.mx (H.M.); velez.edna@icf.unam.mx (E.V.-V.)
- ² Centro de Investigación en Ingeniería y Ciencias Aplicadas, Universidad Autónoma del Estado de Morelos, Av. Universidad 1001, Col. Chamilpa, Cuernavaca 62209, Mexico; arturo_molina@uaem.mx (A.M.)
- ³ Laboratorio de Nanomateriales, Centro Conjunto de Investigación en Química Sustentable, UAEMex-UNAM, Carretera Km. 14.5, Unidad San Cayetano, Toluca-Atlaomulco, Toluca de Lerdo 50200, Mexico; elira@uicol.mx
- ⁴ Laboratorio de Biología de Células Troncales, Facultad de Medicina, Universidad Autónoma del Estado de Morelos, Calle Leñeros s/n, Col. Los Volcanes, Cuernavaca 62350, Mexico
- * Correspondence: sergio.gonzaga@icf.unam.mx

Abstract: In the present work, the powder metallurgy (PM) technique was used to synthesize biocompatible alloys Mg95–Zn5, Mg90–Zn10, and Mg85–Zn15 (wt %) under an argon atmosphere that employed stainless-steel vessels and spheres with a milling treatment of 360 rpm during 15 h. The obtained powder was consolidated through a sintering process for subsequent ion nitriding treatment to increase its corrosion resistance and hardness. The synthesized alloys analyzed by Scanning electron microscopy (SEM) images showed a reduction in particle size with increasing grinding time. The X-ray diffraction (XRD) results showed the formation of a MgZn intermetallic phase and, furthermore, that no impurities were found during the grinding process. The surface-modified Mg–Zn alloys showed some improvement in terms of corrosion (E_{corr} 26% and I_{corr} 13%) and microhardness (HV 40%) compared to Mg. Cytotoxicity evaluation was conducted via an MTT ((3-(4,5-DIMETHYLTHIAZOL-2-YL)-2,5-DIPHENYLTETRAZOLIUM BROMIDE)) assay, which revealed that the Mg–Zn alloys and nitrided samples did not exhibit cytotoxicity towards fibroblast cells after 96 h.

Keywords: biomaterials; mechanical alloying; magnesium alloys; nitriding



Citation: Gonzaga, S.; Molina, A.; Guardian, R.; Martínez, H.; Vázquez-Vélez, E.; Lira-Díaz, E. Superficial Modification of the Mg–Zn Biomaterials via Ion Nitriding for Biomedical Applications. *Metals* **2024**, *14*, 203. <https://doi.org/10.3390/met14020203>

Academic Editor: Erlin Zhang

Received: 14 January 2024

Revised: 31 January 2024

Accepted: 4 February 2024

Published: 6 February 2024



Copyright: © 2024 by the authors. Licensee MDPI, Basel, Switzerland. This article is an open access article distributed under the terms and conditions of the Creative Commons Attribution (CC BY) license (<https://creativecommons.org/licenses/by/4.0/>).

1. Introduction

Currently, biodegradable metals are the most important materials being considered for the manufacture of temporary implants. These materials progressively degrade over time after implantation, which allows avoiding a subsequent second operation to remove the implant. The main property of these materials is they have nearly identical biological and mechanical properties to those of human tissue. In general, biomedical applications use ceramics, polymers, and metals as biodegradable materials. Biomaterials made from ceramic and polymers have been extensively studied; however, because their mechanical properties are not as good as those of human bone, they are not taken into consideration for the creation of degradable implants [1]. Recently, biodegradable metallic implants have increased interest between scientists [2–4]. Magnesium (Mg), zinc (Zn), and iron (Fe) are specific examples of widely researched biodegradable materials [5,6]. Of the aforementioned metals, magnesium and its alloys are more suitable candidates for biodegradable materials than other polymeric and metallic biomaterials, and they have thus attracted attention for application as temporary implants [7–10].

Mg biocompatibility plays an important task in sustaining metabolism by releasing Mg ions during the degradation of Mg implants. For magnesium ions, no negative effects

have yet been documented. Additionally, the elastic modulus of magnesium (40–45 GPa) is closer to that of natural bone (3–20 GPa) than it is to metallic materials like titanium alloys, cobalt-based alloys, and stainless steels [11,12]. Post-implantation studies of Mg biomaterials indicate Mg has good biocompatibility and its degradation products are not toxic to the human body [13–17]. However, there are serious concerns regarding the accelerated corrosion behavior of Mg-based alloys, such as H₂ buildup, alkalinization of body fluids, and mechanical failure before fulfilling the intended purpose of an implant [18]. Despite such problems, research is still being carried out in the domain of the manufacturing design and composition of magnesium-based materials.

Mechanical alloying (MA) is a technique by which advanced materials with different properties can be processed. Due to the microstructural refinement to which the precursor powders are subjected in the grinding process, mechanical alloying has positioned itself as a versatile technique in the manufacture of new materials, and therefore, it is an appropriate technique for manufacturing magnesium-based materials and high-melting-point alloys [19]. Recently, numerous reports have been made about the surface modification of Mg alloys and their ability to protect against corrosion through the formation of biocompatible coatings [20–28], improving the degradation rate in a physiological environment to favor the cell growth and be used for application as an implant. The methods to control an undesirably high degradation rate include surface coatings, such as laser cladding, magnetron sputtering, and nitriding [29], which have been used to improve the surface properties of materials. Developing a biocompatible and bioactive protective coating is an attractive way to slow the degradation rate of Mg alloys; in general, ion nitriding has been used to successfully enhance the wear and corrosion resistance of materials [29]. Coatings protect the substrate by providing a barrier between the metal and its environment and/or by the presence of corrosion-inhibiting chemicals in them. Consequently, we selected ion nitriding as it is a process that uses a direct current (DC) discharge to ionize a mixture of nitrogen-enriched gases and modify the microstructure of the synthesized Mg–Zn alloys, which is useful for applications such as temporary implants since the gas used is noble and does not form chemical compounds that are harmful to the human body and this helps to have better cell growth in the damaged area or in areas that need to be repaired.

In the present work, Hank's solution corrosion behavior of Mg–Zn alloys superficially modified by ion nitriding was studied. The corrosion behavior was characterized by polarization curves (E_{corr} and I_{corr}). Cytotoxicity tests were carried out on all samples using human fibroblasts as the cell line. The results obtained demonstrated that the materials used in this type of cell did not induce toxicity. It is expected this research will help study the behavior of nitriding in Mg-based alloys and their possible use as a temporary implant.

2. Materials and Methods

The alloys Mg95–Zn5, Mg90–Zn10, and Mg85–Zn15 (% by weight) were manufactured using the mechanical alloying (MA) technique. The raw materials in this experiment were Mg and Zn powders with average diameters of around 40.0 μm and 15.0 μm (Figure 1) and a purity of 99.8% and 99.6%. The powder obtained through mechanical alloying was uniaxially compacted into a cylindrical die using a hydraulic press at a pressure of 500 MPa and with a residence time of 5 min. A green compact 0.0127 m in diameter was obtained, which was then sintered in an argon atmosphere at 400 °C, obtaining solid and rigid samples for subsequent ionic nitriding for 5 h to improve the properties of the Mg–Zn alloys. Vickers microhardness (HV) tests were carried out on the Mg–Zn alloys and nitrided samples, applying a load of 0.2 kg with a time of 25 s.

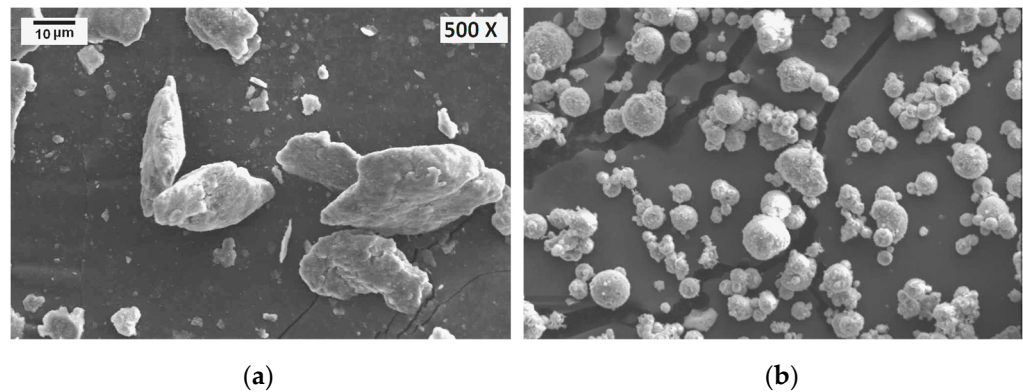


Figure 1. Original powders (a) Mg and (b) Zn.

2.1. Microstructure and Composition

The microstructure and corrosion products of the different samples were observed by scanning electron microscopy (SEM) paired with energy-dispersive spectroscopy (EDS) with a voltage of 20 kV. The sample phases were characterized by X-ray diffraction (XRD) using CuK α radiation with a wavelength of 1.5406×10^{-10} m.

2.2. Ion Nitriding

Ion nitriding is a process of plasma-activated thermochemical diffusion used for surface hardening of ferrous and non-ferrous metals [30]. This process is carried out in a vacuum chamber, where the working sample is directly connected to a cathode. A high potential is then applied between the cathode and the walls of the chamber, which functions as the anode, by which plasma is produced in a gaseous mixture, usually under a low vacuum (0.75–10 Torr). The samples used were the sintered alloys Mg95–Zn5, Mg90–Zn10, and Mg85–Zn15, which were polished with SiC sandpaper (2000 grit). Ion nitriding was carried out using nitrogen gas for 5 h in a pulsed DC discharge plasma reactor.

2.3. Electrochemical Tests

The working area of the electrochemical samples was 0.0127 m, and the surface of the Mg–Zn alloys was polished with SiC sandpaper (2000 grit). Electrochemical tests were performed in a beaker containing Hank's solution (0.80 g/L NaCl, 0.14 g/L CaCl₂, 0.40 g/L KCl, 0.35 g/L NaHCO₃, 1.00 g/L glucose, 0.10 g/L NaH₂PO₄, 0.10 g/L MgCl₂·6H₂O, 0.60 g/L Na₂HPO₄·2H₂O, and 0.06 g/L MgSO₄·7H₂O) [31] and a standard configuration of three electrodes (saturated Ag/AgCl reference electrode, graphite electrode as the counter electrode, and Mg–Zn alloys and nitrided samples as the working electrodes) at 37 °C. The results of the corrosion potential (E_{corr}) and the corrosion current density (I_{corr}) were evaluated using the Tafel extrapolation method [32]. The corroded samples were rinsed with distilled water and dried using flowing air to subsequently perform EDS coupled to the SEM.

2.4. Cytotoxicity Test

Cytotoxicity testing of the samples was carried out according to ISO 10993-12 [33]. The cytotoxicity assays were done via indirect contact with fibroblasts (ATCC PCS-201-010). Fibroblast cells were cultured in Dulbecco's modified Eagle's medium supplemented with 10% fetal bovine serum (Biowest, cat. S1650), 1% antibiotic–antimycotic (Gibco, cat. 15240062), 2 mM glutamine (Gibco, cat. 25030081), and 1% sodium pyruvate (Gibco, cat. 11360070) in a 5% CO₂ incubator at 37 °C. The Mg–Zn alloys were polished with SiC sandpaper (2000 grit). All of the samples were put in 15 mL Falcon tubes at 25 °C after being sterilized for 30 min on both sides with UV light. The previously sterilized samples were treated with the fibroblast growth medium for 24 h at 37 °C in a 5% CO₂ atmosphere in order to prepare the extracts. The extracts were centrifuged to get rid of

any deteriorated material. Prior to cytotoxicity testing, the supernatant was aspirated and kept in a refrigerator at 4 °C. The concentration of the extract was diluted to 25%, 50%, 75%, and 100%. Subsequently, three extract samples for each extract were individually put onto 96-well cell culture plates (5×10^4 cells/100 μ L media), and the cells were allowed to proliferate for 96 h. Three duplicates of the experiments were carried out. Light microscopy was used to observe the morphology of the cell growth, and the MTT test was used to assess the viability of the fibroblast cell. The relative growth rate (RGR) was estimated employing Equation (1), where OD is optical density.

$$(\text{RGR} = \text{Experimental Group OD Mean} / \text{Negative Control Group OD Mean} \times 100\%) \quad (1)$$

3. Results

Figure 1 displays the SEM micrographs of the original powders. Mg has a primarily flake-like morphology, while Zn has a spherical form.

3.1. Scanning Electron Microscopy

Figures 2–4 show the size and morphology of the particles as the grinding time is increased. SEM micrographs (Figures 2d, 3d and 4d) of the Mg95–Zn5, Mg90–Zn10, and Mg85–Zn15 powders reveal that next 15 h of grinding, two kinds of deformation mechanisms during milling can be observed: ductile deformation, where flat particles are formed through elongation; and brittle deformation, which outcomes in the formation of angular and irregular particles typical of brittle materials.

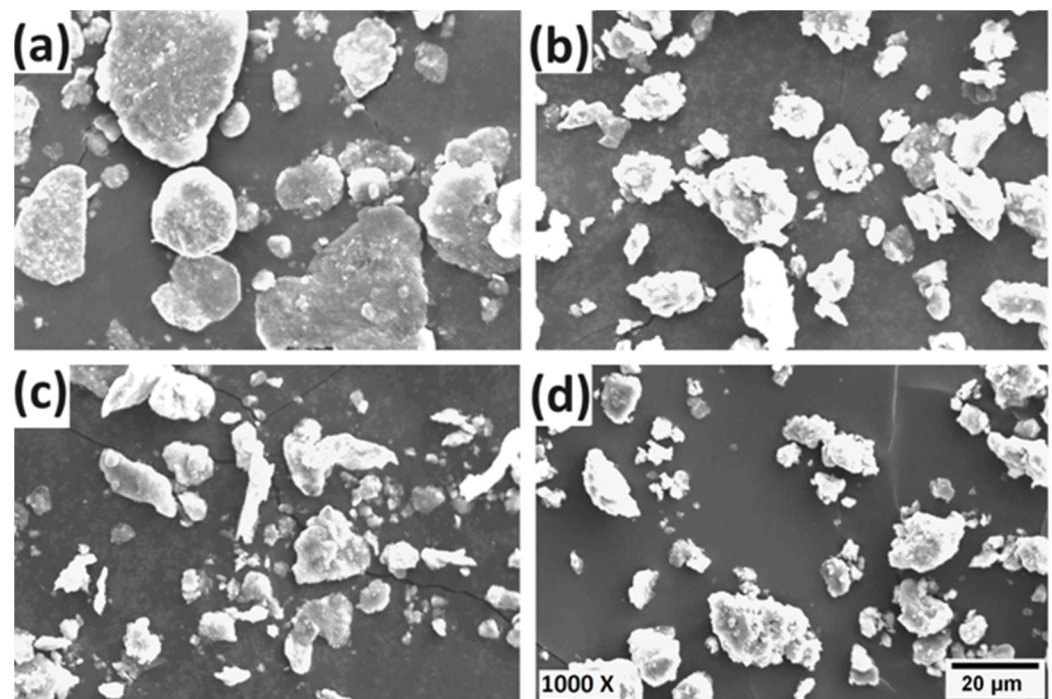


Figure 2. SEM micrographs of the milled Mg95–Zn5 at (a) 2, (b) 5, (c) 10 and (d) 15 h.

SEM micrographs of the powder mixtures after 15 h of milling (Figures 2d, 3d, and 4d) showed a decrease in particle size compared with the tests milled for 2 h (Figures 2a, 3a, and 4a). Flattening of particles, cold welding, plastic deformation of welded particles, and fractures are phenomena that occur continuously during the mechanical alloying process. In the mechanical alloying process, atom interdiffusion in the welded layers dominated over self-diffusion in the present elements, and this is due to the high impact energy and temperatures generated during grinding.

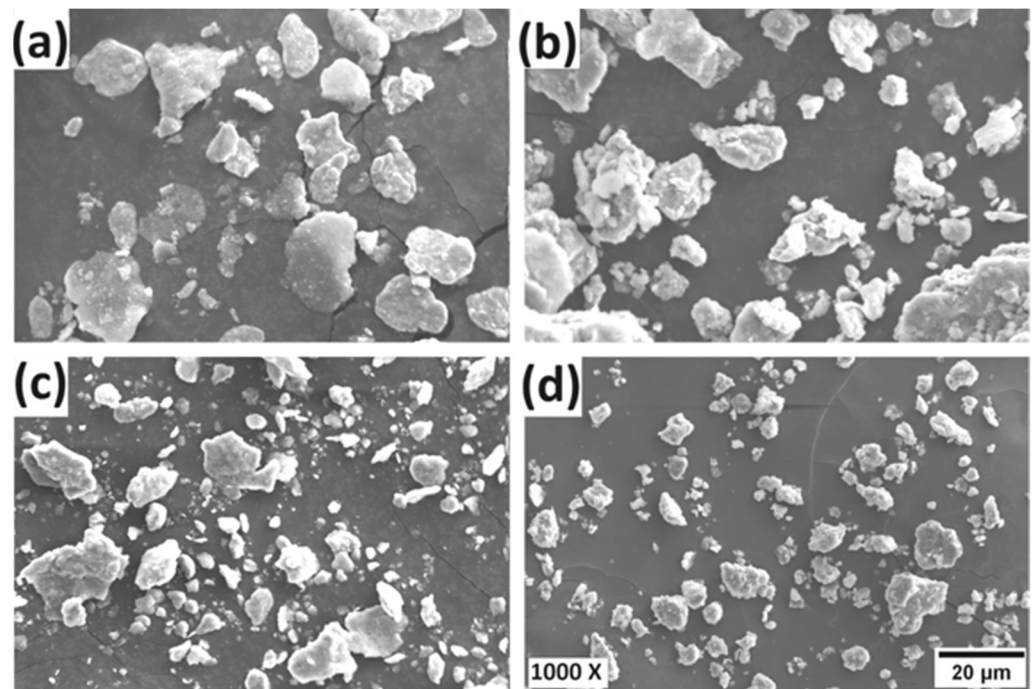


Figure 3. SEM micrographs of the milled Mg90–Zn10 at (a) 2, (b) 5, (c) 10 and (d) 15 h.

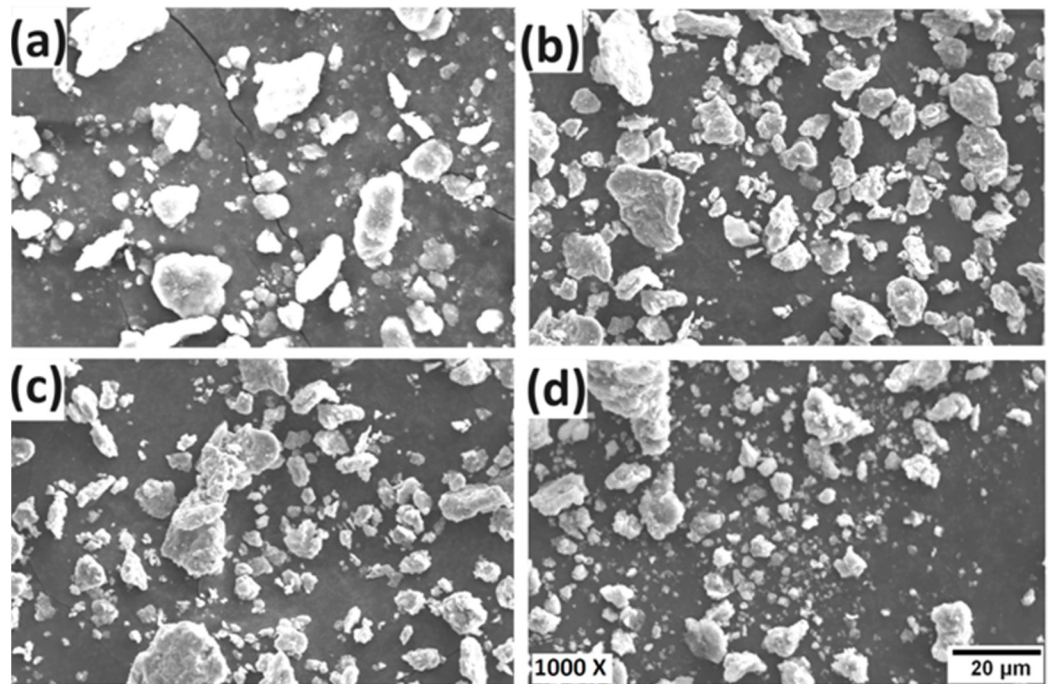


Figure 4. SEM micrographs of Mg85–Zn15 milled for (a) 2, (b) 5, (c) 10 and (d) 15 h.

Figure 5a shows the evolution of particle size as the milling time progressed for Mg95–Zn5. Consequently, after 2 h of milling, the average particle size was between 7 and 15 μm , and between 3 μm and 7 μm after 15 h of milling. For Mg90–Zn10 (Figure 5b), the average particle size was between 8 μm and 12 μm after 2 h of milling and decreased after 15 h, varying in the range of 4–8 μm . For Mg85–Zn15 (Figure 5c), the average particle size was between 6 μm and 10 μm after milling 2 h and decreased after 15 h, varying in the range of 2–5 μm .

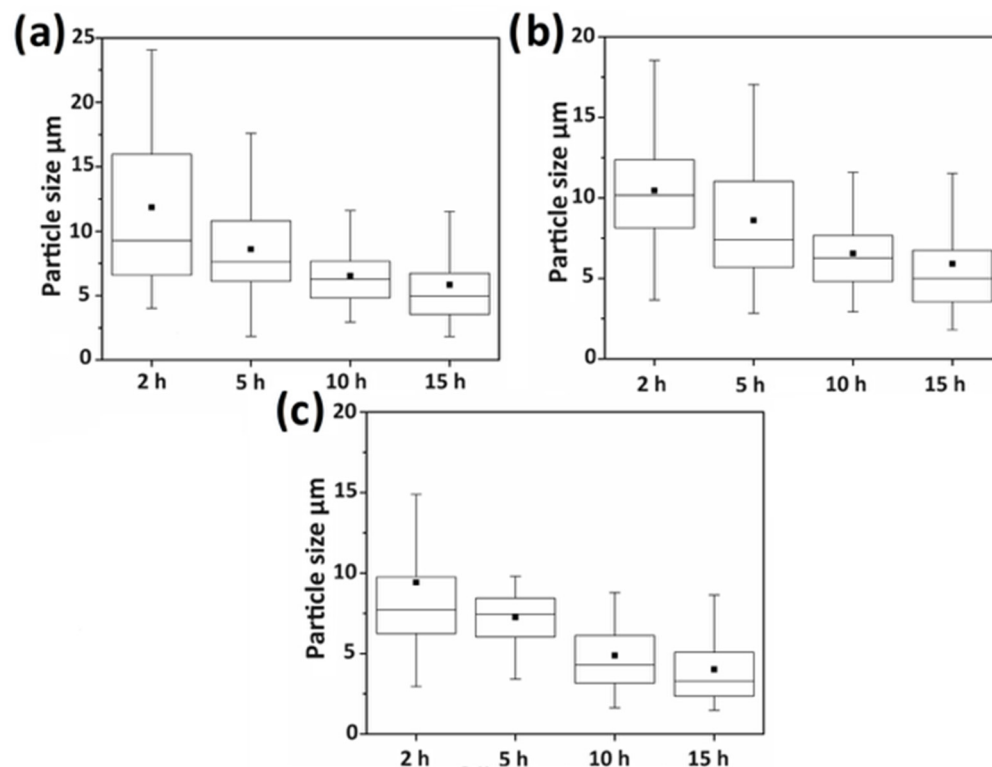


Figure 5. Particle size evolution of (a) Mg95–Zn5, (b) Mg90–Zn10, and (c) Mg85–Zn15 for 2, 5, 10, and 15 h of milling time.

3.2. X-ray Diffraction

Figures 6–8 show the diffractograms for the Mg95–Zn5, Mg90–Zn10, and Mg85–Zn15 powders after 2, 5, 10, and 15 h of grinding. In the three compositions at the initial grinding time, Mg (COD # 9008506) [34] was observed as the element that generates the most intense peaks, except after 5 h of grinding, where peaks with less intensity and slightly displaced from the initial Mg are detected—at this grinding time, Zn (COD # 9008522) [34] has been integrated into Mg through the mechanical grinding process. The decrease in intensity is produced by amorphization occurring between 10 and 15 h of grinding, giving way to changes in the structure.

In the evolution of the diffractograms, the development of a MgZn intermetallic phase [35] is observed a few hours after grinding. In addition, as the grinding time progresses, partial amorphization is apparent in the diffraction peaks for the three compositions. The diffractograms of the initial samples for the three compositions shown in Figures 6–8 show well-defined peaks characteristic of the crystallinity of the present elements, and as the grinding time progresses, the diffractograms reveal a decrease in the intensities of the diffraction peaks and their widening, which indicate a decrease in the size of crystallites and an increase in internal stresses [36]. This trend increases with the extension of grinding time. In addition, shifts in angles were also caused by a reduction in crystallite size and lattice strain buildup during mechanical alloying, indicating the fine crystallite formation was typically affected by the increasing number of collisions per unit of time during the milling process [36,37]. This is associated with the occurrence of two types of phenomena in the grinding process: the solubility of Zn in the Mg lattice and the size refinement of the Mg and Zn particles, which makes analysis by XRD difficult due to poor detection. Due to the temperature produced during the mechanical process and the amount of magnesium used, the phase or possible phases formed are MgZn and Mg7Zn3 [38], but in this work, only the intermetallic phase MgZn was obtained.

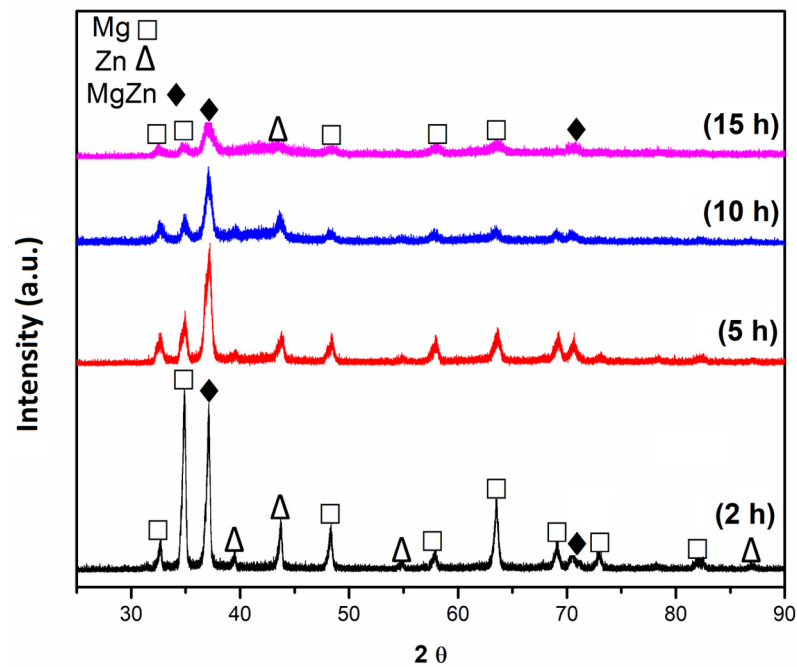


Figure 6. XRD patterns of the milling Mg₉₅-Zn₅ at 2, 5, 10, and 15 h.

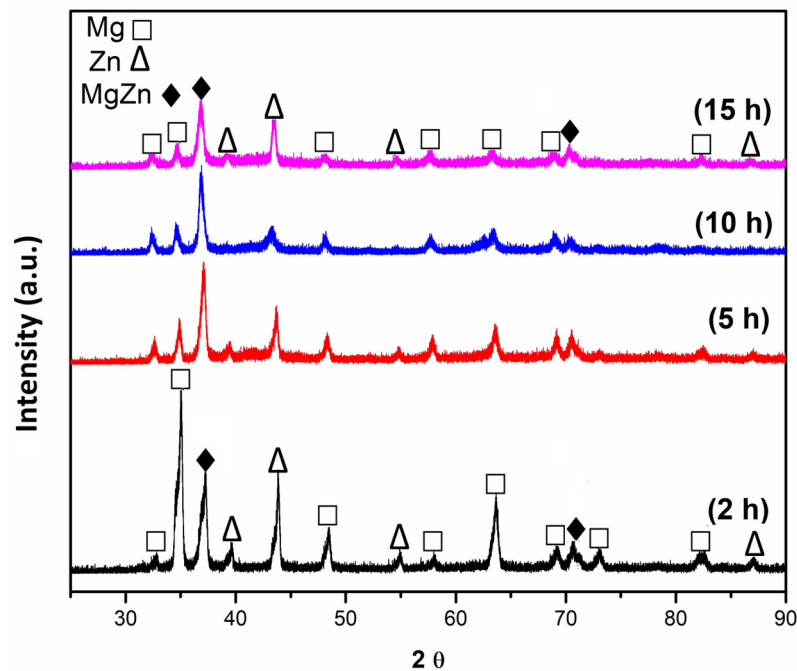


Figure 7. XRD patterns of the milling Mg₉₀-Zn₁₀ at 2, 5, 10 and 15 h.

3.3. Sintering

The diffractograms of the powders of the Mg–Zn alloys for the three compositions as the grinding time passes (Figures 6–8), a decrease in the size of the peaks and a certain amorphicity of these are observed because a decrease in size occurred of crystallite. There was deformation in the crystalline network, all this is related to the collisions suffered during the grinding process. Still, the XRD of the sintered samples (Figure 9) showed some certain crystallinity and an increase in the intensity of the peaks, these are due to the energy supplied during the sintering treatment which causes the atoms of the crystallized network to be ordered and that makes their detection by XRD easier. Figure 10 shows the micrographs of the Mg–Zn alloys cold compacted and sintered at 400 °C for 3 h. The

sintered Mg–Zn samples presented a good union and distribution between the Mg matrix and the Zn particles as a result of the effect of the pressure and temperature applied during the sintering process, which causes the porosity of the particles to decrease due to the union of these during the sinetrization treatment.

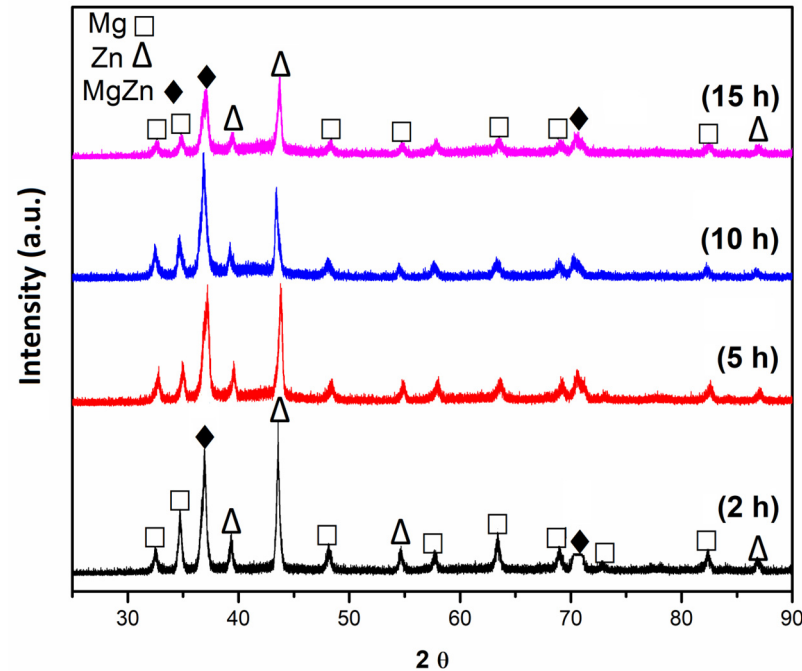


Figure 8. XRD patterns of the milling Mg85–Zn15 at 2, 5, 10 and 15 h.

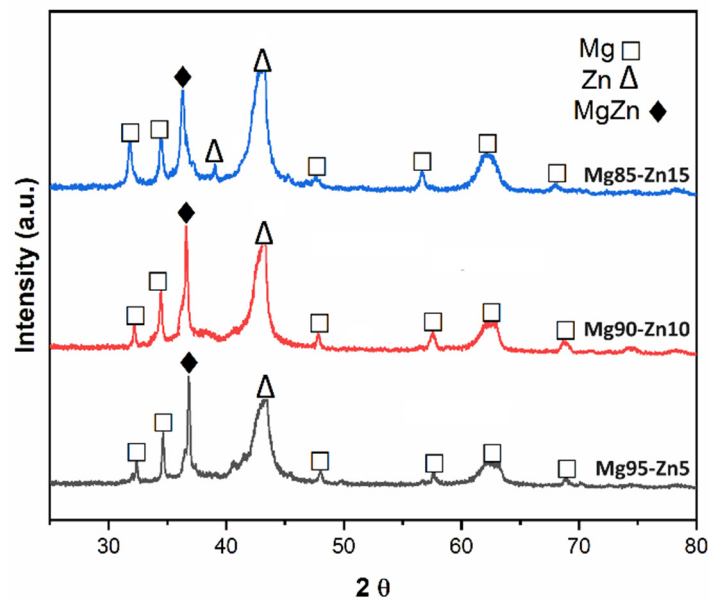


Figure 9. XRD patterns of sintered samples.

3.4. Ion Nitriding

The nitrated samples were subjected to different analyses to verify the results of the ion nitriding treatment as follows: the appearance of the modified layer was observed using a scanning electron microscope (Figure 11). In order to verify the results, the samples were cut transversely, and the samples were observed at a magnification of $2000\times$ (Figure 12) with subsequent EDS analysis, obtaining results for Mg, Zn, N, and O (Figure 13). Figure 12 shows the nitrated samples, and a homogeneous layer can be observed in the upper part

of the micrographs. It was found that all the samples had a similar structure but different layer thicknesses. The EDS distribution results of the corresponding cross-section reveal that Mg gradually diffused from the substrate to the surface, which is mainly attributed to the strong diffusivity of Mg with nitrogen and the formation of Mg nitrides. No peaks of nitrides or corrosion products appear in the XRD results as the low volume amount of these <1 vol% is below the technique's detection limits.

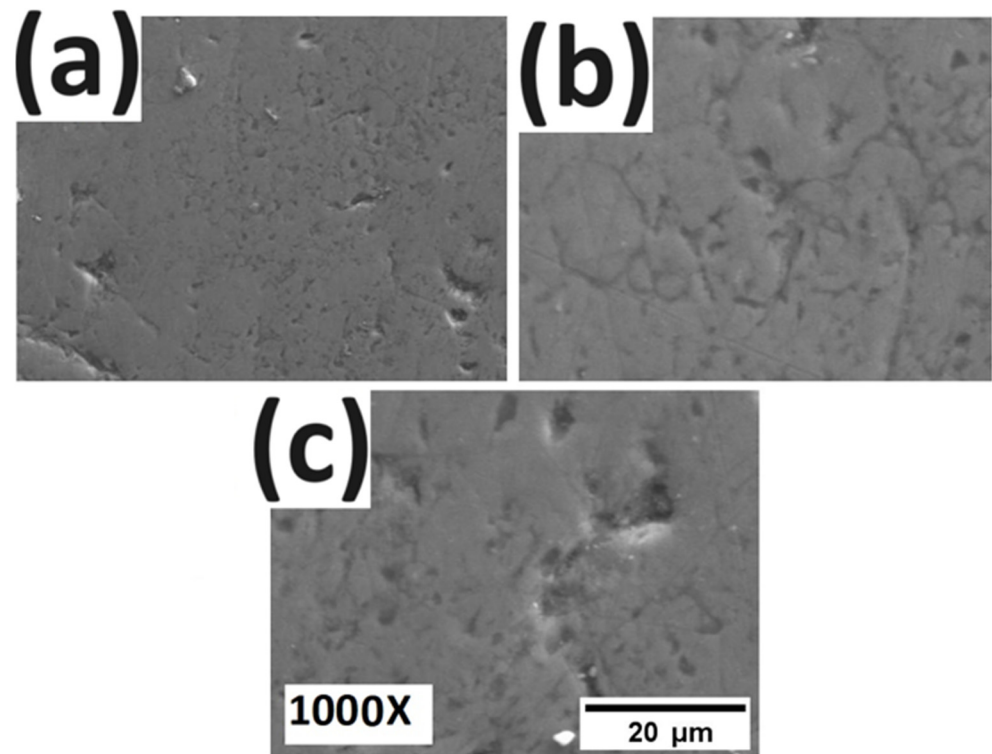


Figure 10. Sintered samples (a) Mg₉₅-Zn₅, (b) Mg₉₀-Zn₁₀, and (c) Mg₈₅-Zn₁₅.

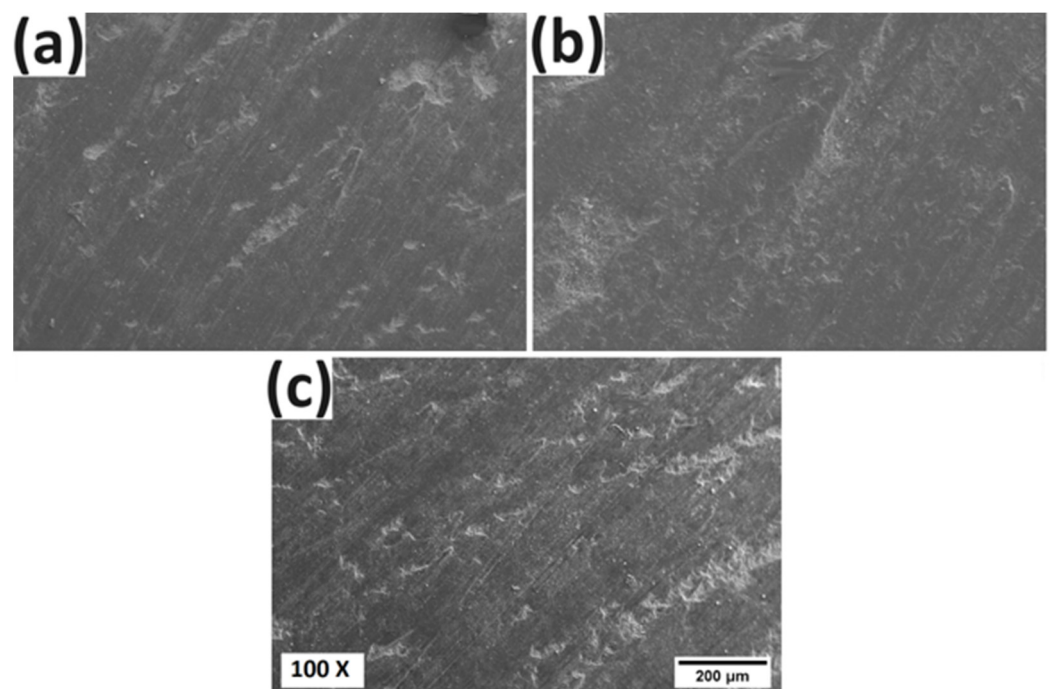


Figure 11. Nitrided samples, (a) Mg₉₅-Zn₅, (b) Mg₉₀-Zn₁₀, and (c) Mg₈₅-Zn₁₅.

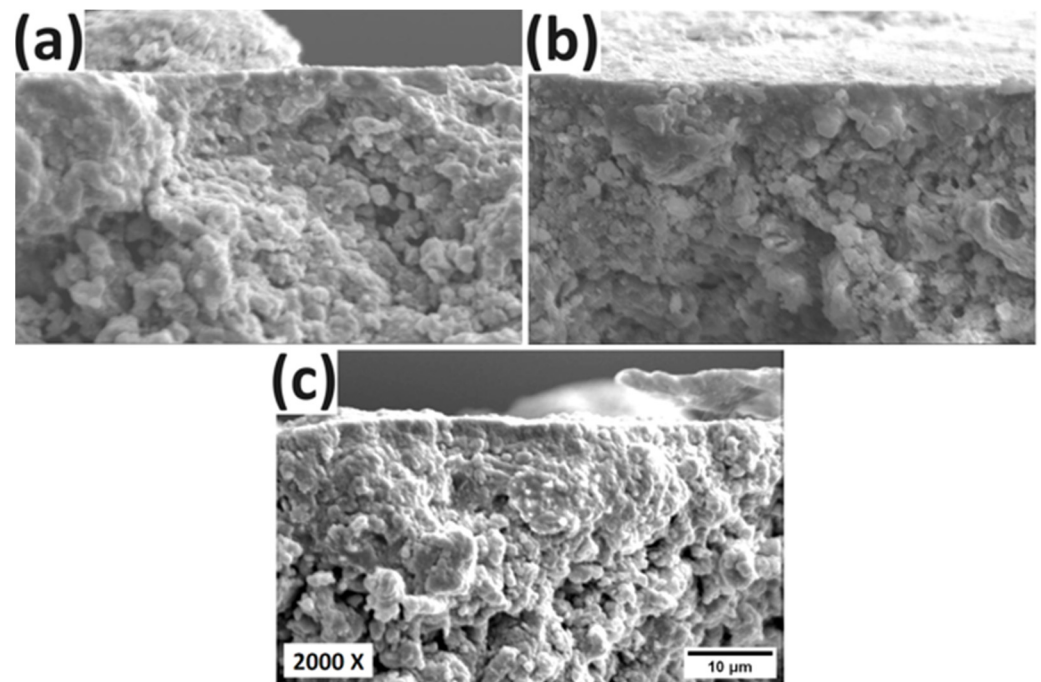


Figure 12. Cross-section of the nitrided samples: (a) Mg95–Zn5, (b) Mg90–Zn10, and (c) Mg85–Zn15.

3.5. Potentiodynamic Polarization Curves

Figure 14 shows the potentiodynamic polarization curves of the samples used in Hank's solution, and it can be seen that the corrosion potential for the nitrided samples has slightly shifted in the positive direction, indicating an increase in their corrosion resistance compared to Mg–Zn alloys and Mg. The corrosion current density values of the nitrided samples were lower than those of the Mg–Zn alloys and Mg. These results suggest that nitride coatings significantly improve the corrosion resistance of Mg–Zn alloys in Hank's solution by retarding the cathodic reaction. Such behavior could be attributed to the formation of a protective layer over the active cathodic sites on the surface. The E_{corr} and I_{corr} data generated from the potentiodynamic polarization tests are presented in Table 1.

Table 1. E_{corr} and I_{corr} .

Sample	E_{corr} (mV)	I_{corr} (mA/cm ²)
Mg	−1428	0.166
Mg95–Zn5	−1343	0.069
Mg90–Zn10	−1258	0.038
Mg85–Zn15	−1242	0.053
Nitrided: Mg95–Zn5	−1232	0.080
Nitrided: Mg90–Zn10	−1136	0.026
Nitrided: Mg85–Zn15	−1131	0.022

From the results of the polarization curves, the corrosion resistance of all the nitrided samples shows a more pronounced effect in terms of corrosion resistance. The surfaces of the corroded samples were examined to investigate the corrosion behavior further. Figure 15 shows the morphology of the corroded surface of the alloys and nitrided samples, where many corrosion products can be seen accumulating in agglomerates and are unevenly stacked on the substrate surface. In Figure 15, various marks of holes, cracks, and other defects are seen show in and over the corroded area. Those corrosion products are expected to not exert an appropriate protective impact on the alloys and nitrided samples.

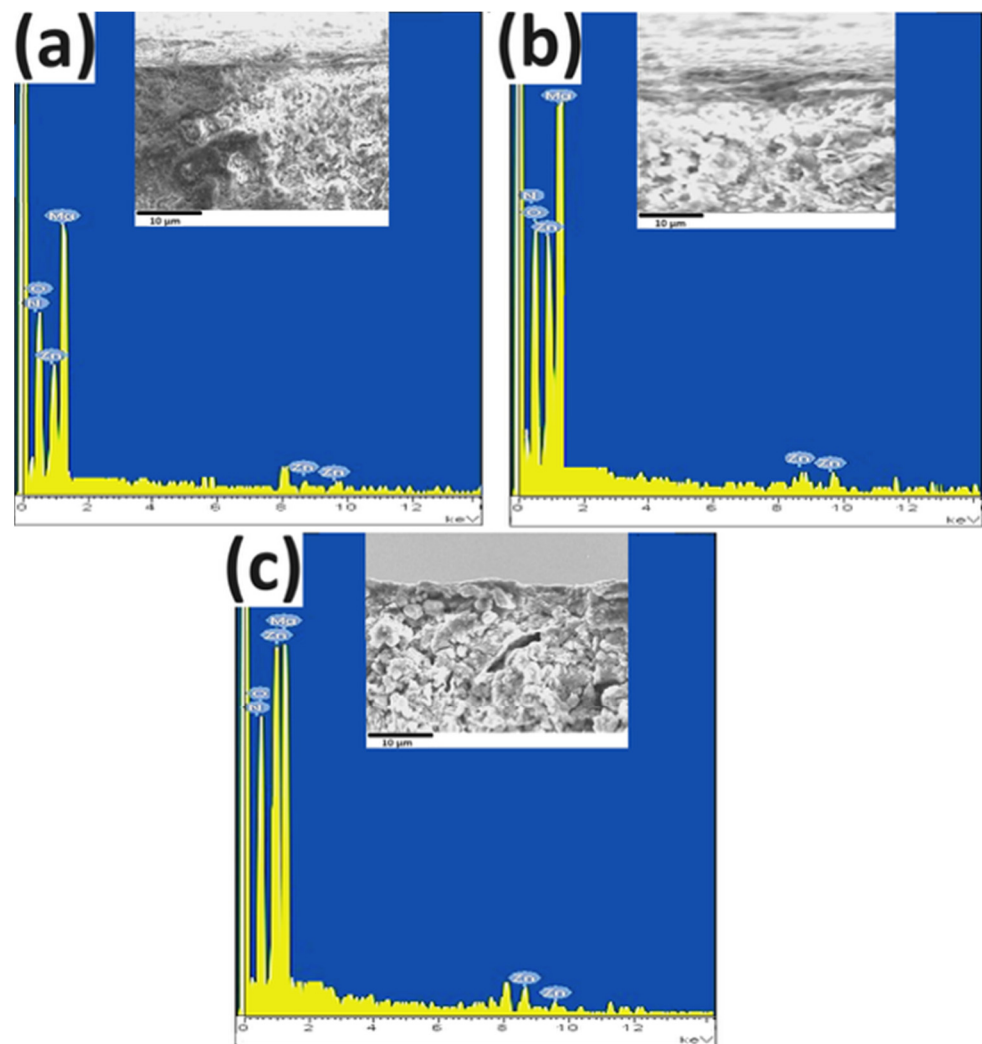


Figure 13. SEM–EDS at the cross-section of the nitrided samples: (a) Mg95–Zn5, (b) Mg90–Zn10, and (c) Mg85–Zn15.

The EDS results of the corroded areas of the samples used showed that the corrosion products consist of elements Mg, O, Cl, P, Zn, Ca, and Na (Figure 16). Due to the components of Hank’s solution, it is difficult to know the corrosion products, but it has been determined that they are composed of $\text{Mg}(\text{OH})_2$ [39]. In Hank’s solution, Cl adsorbed onto the Mg surface readily transforms $\text{Mg}(\text{OH})_2$ into soluble MgCl_2 [39], destroying the corrosion product cup and causing pitting corrosion. Hydrogen gas is generated by the local cathodic reaction forces breaking and separating in the coating, resulting in corrosion products accumulating at the coating–substrate interface, coating material partially peeling off from the substrate, and the substrate eventually losing its protection [40]. Figure 15e–g present the corrosion morphologies of the nitrided samples after electrochemical corrosion tests, where various types of corrosion pitting are evident due to the effect of Cl penetration during corrosion, while other areas remain intact and undamaged. Compared to the nitrided samples and Mg–Zn alloys, there is obviously reduced pitting corrosion in the nitrided sample, and in terms of surface quality, there are more intact undamaged areas. It is observed that the corrosion resistance has been further improved by the nitriding treatment, which agrees well with the results of the polarization curves in Figure 14.

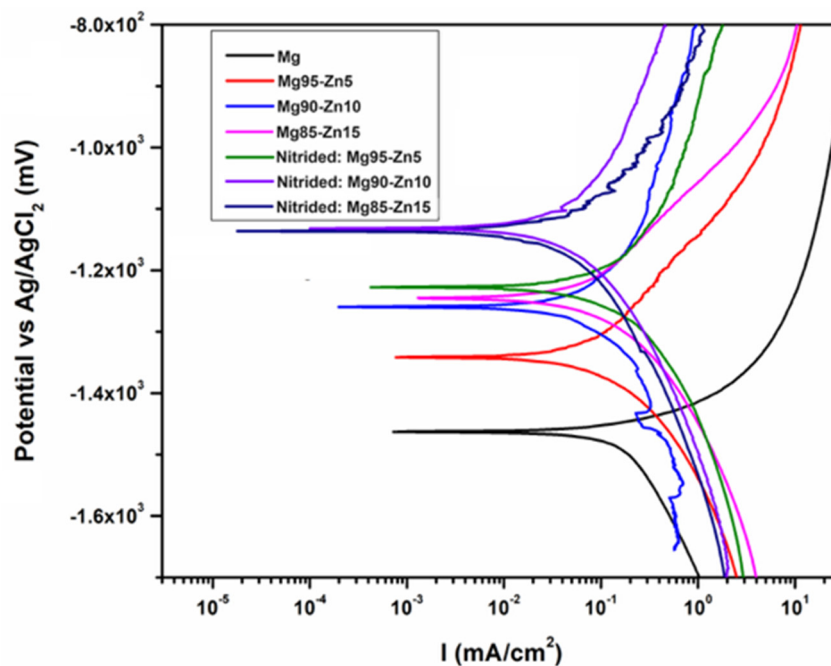


Figure 14. Potentiodynamic polarization curves.

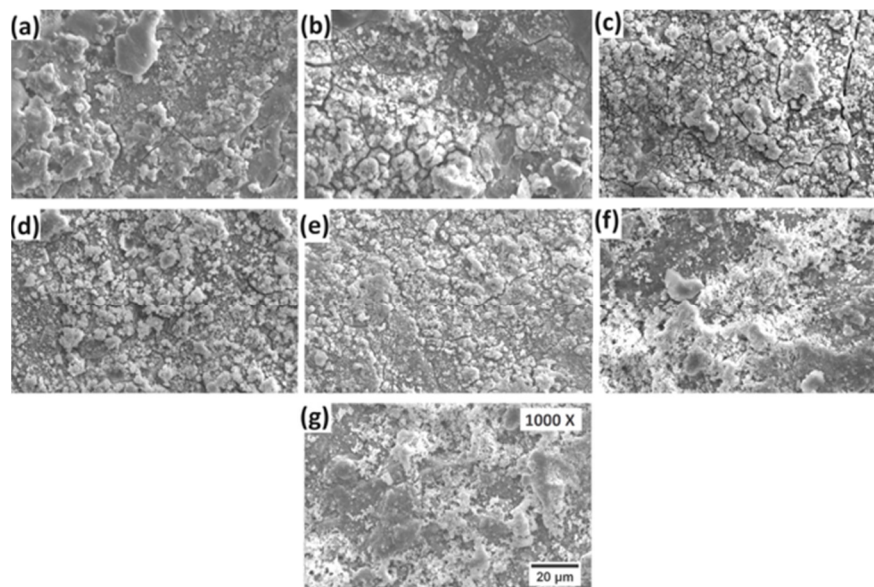


Figure 15. SEM micrographs of (a) Mg, (b) Mg95–Zn5, (c) Mg90–Zn10, (d) Mg85–Zn15, (e) nitrided Mg95–Zn5, (f) nitrided Mg90–Zn10, and (g) nitrided Mg85–Zn15 after the potentiodynamic polarization tests.

3.6. Cytotoxicity Test

Figure 17 shows the cell viability of the fibroblasts after incubation for 96 h. In the case of the solutions containing 100% extract, the dendrite-shaped cells attached after incubation for 96 h proliferate comparably to the control (Figure 18), consistent with the RGR results (Figure 17). Figure 18 indicates that fibroblast cells can proliferate normally in solutions of the extracts Mg, Mg95–Zn5, Mg90–Zn10, Mg85–Zn15, nitrided Mg95–Zn5, nitrided Mg90–Zn10, and nitrided Mg85–Zn5, exhibiting good cytocompatibility. There was a greater increase in cell viability with the decrease in extract concentration, indicating that the extracts promote cell growth. The RGR results for the tested samples indicate that they are not toxic to fibroblast cells and, thus, could be considered for use in biomedical applications.

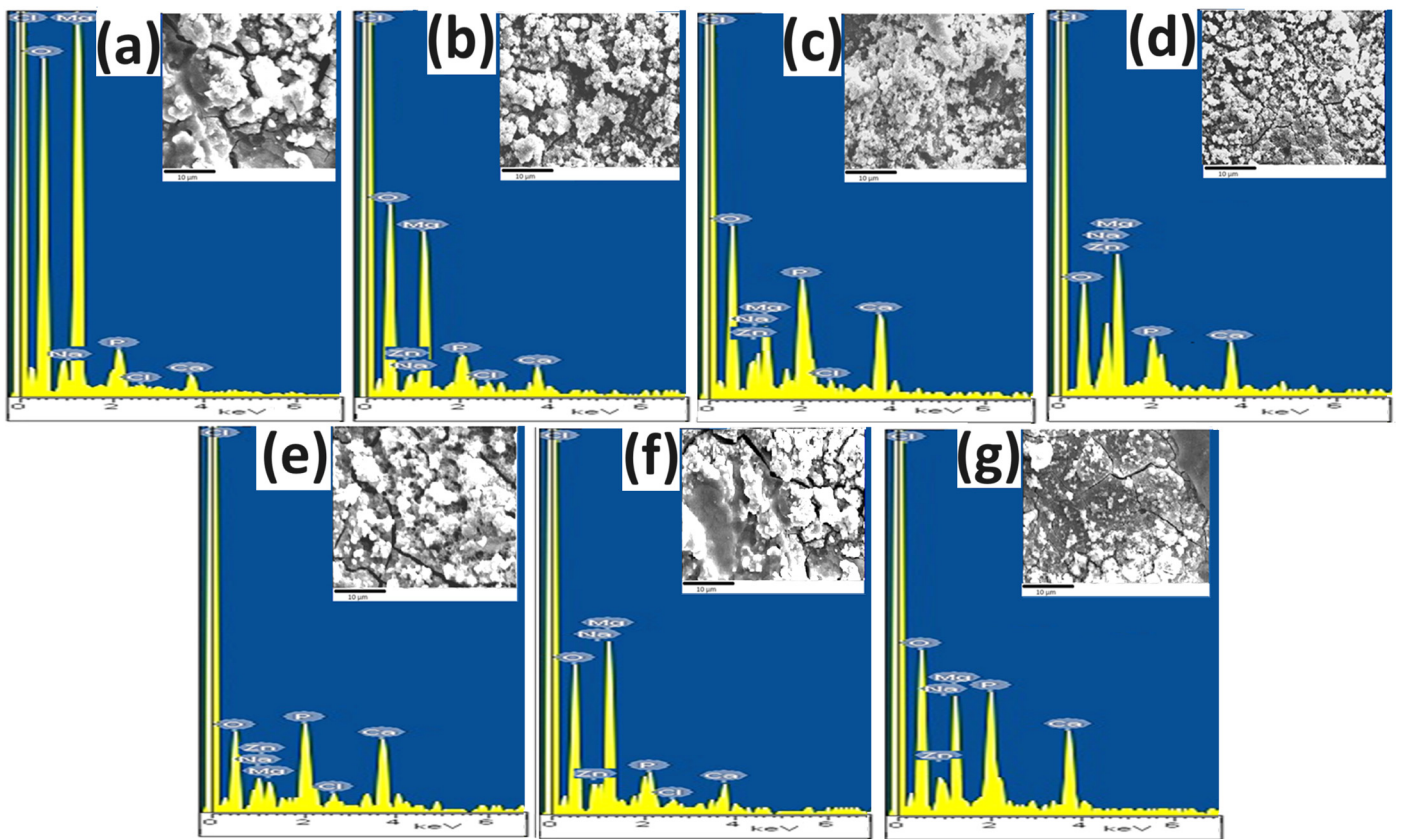


Figure 16. SEM-EDS (a) Mg, (b) Mg95-Zn5, (c) Mg90-Zn10, (d) Mg85-Zn15, (e) nitrided Mg95-Zn5, (f) nitrided Mg90-Zn10, and (g) nitrided Mg85-Zn15 after the potentiodynamic polarization tests.

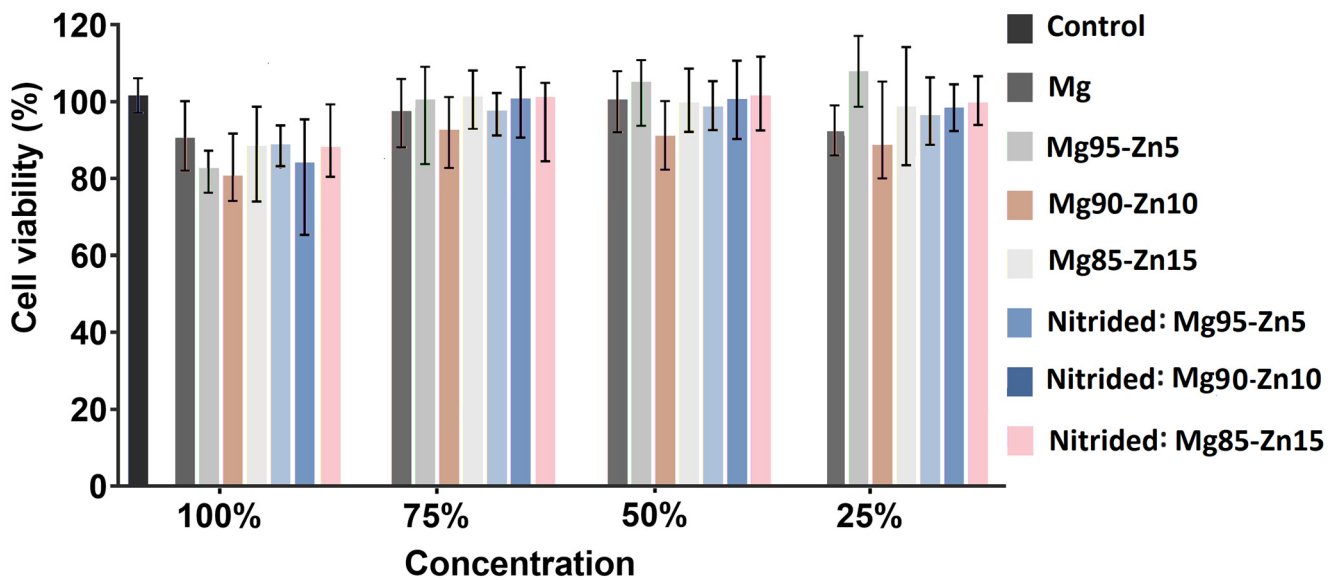


Figure 17. Cytotoxicity test (RGR).

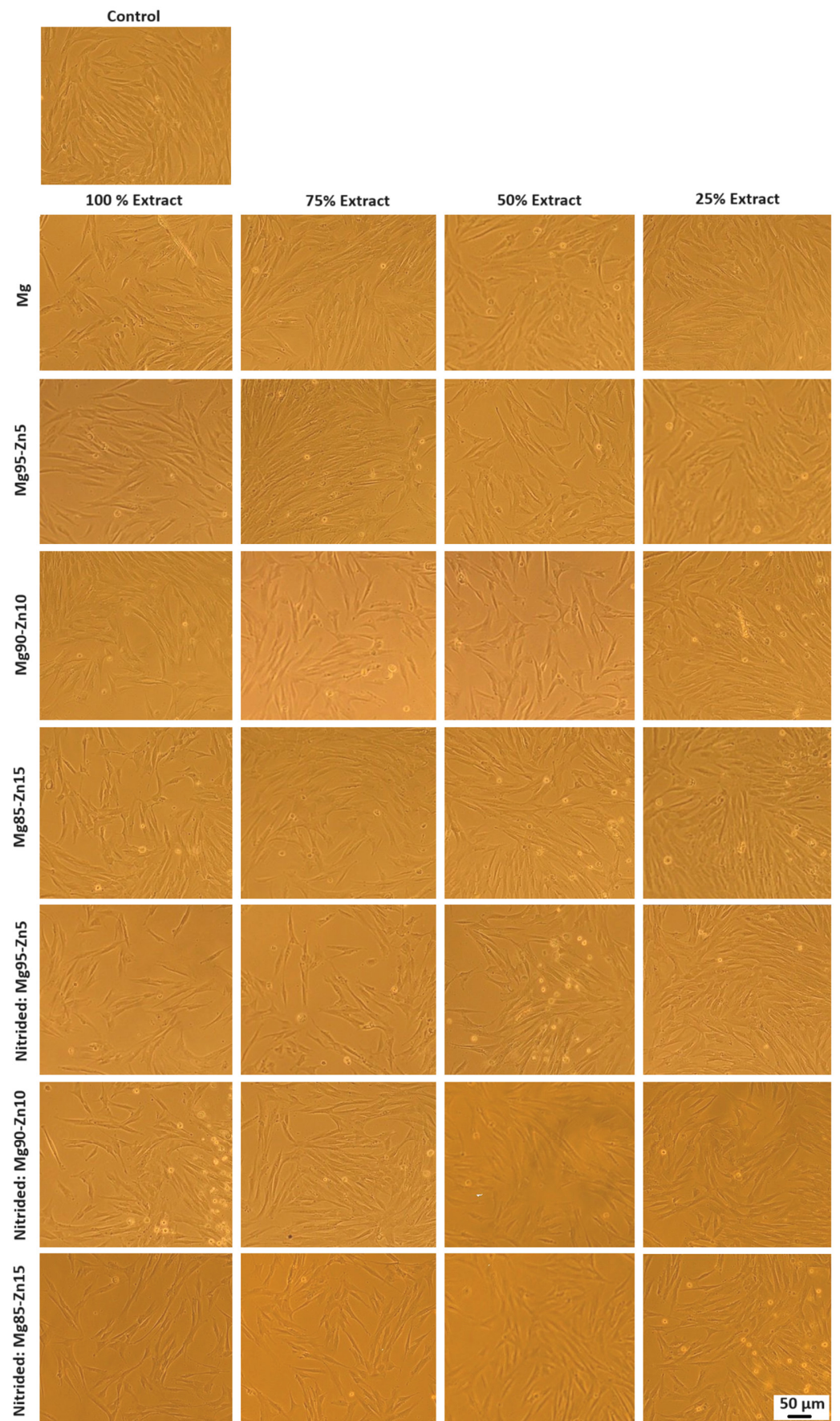


Figure 18. Cultured fibroblasts morphology and proliferation after 96 h (100×).

3.7. Microhardness (HV)

Figures 2–4 show that the particle size decreases with the increase in milling time. The variation in particle size could be attributed to different amounts of plastic deformation and fractures produced in the mechanical milling process. In general, the strength and hardness of the Mg–Zn alloys increase with increasing Zn concentration [41], facilitating better fragmentation of the zinc particles in magnesium during grinding. On the other hand, when the alloy contains a large amount of Mg—that is, a low concentration of Zn—the ductility of the system will be high, and, therefore, particle fragmentation is hindered. Therefore, the particle size decreases with the increasing Zn concentration of the alloys.

Vickers microhardness analysis of the samples was carried out with a test load of 0.2 kg. The results are presented in Table 2, in which a significant increase in the surface hardness of all the nitrided samples is observed in comparison with the Mg–Zn alloys. The increase in hardness is attributed to the growth of Mg nitrides on the surface of the nitrided tests.

Table 2. Microhardness test (HV).

Sample	Vickers Microhardness (HV)
Mg	58.52 ± 3.25
Mg95–Zn5	67.49 ± 2.40
Mg90–Zn10	74.74 ± 2.77
Mg85–Zn15	78.46 ± 3.10
Nitrided: Mg95–Zn5	86.49 ± 3.00
Nitrided: Mg90–Zn10	81.84 ± 3.44
Nitrided: Mg85–Zn15	84.75 ± 2.45

4. Discussion

Analysis of the Mg–Zn alloys produced by mechanical alloying displayed that the particle size decreases as a function of the grinding time (Figures 2–4), which is due to the collisions that give rise to the fracture and welding of the materials used during the milling process, and for this reason, there is a refinement of particle size. XRD showed the different phases existing in the Mg95–Zn5, Mg90–Zn10, and Mg85–Zn15 alloys during the milling process, as seen in Figures 6–8, a MgZn phase is present in all three synthesized alloys, in concordance with previous reports [42]. The results of EDS and XRD analyses carried out in this investigation did not display the presence of Fe impurities or some type of contamination. Previous investigations on the use of Mg-based alloys as bio-degradable materials have shown promising results [43–45]. The results of the potentiodynamic polarization curves of the Mg–Zn alloys and the nitrided samples in Hank’s solution are shown in Figure 14. These results can be compared with various works carried out in which it has been reported that the corrosion potential improved significantly in the nitrided samples presented in this work in comparison with the coatings made by MAO (micro-arc oxidation) on a Mg–Zr alloy [46] in Hank’s solution, and the results obtained in alloys Zn–Mg and Zn–Mg–Y alloys in NaCl solution [47] but not with the corrosion current density which was lower than the nitrided samples. With the corrosion results obtained in this study, it can be deduced that the nitriding coatings increased the corrosion resistance and reduced the substrate due to the protective effect of the nitrided layer [40].

The cytotoxic behavior, as characterized using MTT, showed good cell proliferation in the presence of the realized coatings and the Mg–Zn alloys, demonstrating that the nitrided samples and the Mg–Zn alloys offer a biologically favorable environment, suggesting they are biocompatible and do not induce any toxic effects [48]. Additionally, Figure 18 shows the morphology of cells in the different extracts, which is similar to that of the control, indicating that they were healthy, and these conclusions are supported by the results obtained from the RGR graphs. Therefore, indirect cytotoxicity assays are suitable for investigating the effects on cell proliferation and viability resulting from elements released by Mg–Zn alloys and nitrided samples. It can be seen from Table 2 that the nitrided samples

have higher microhardness values than the synthesized alloys, and this is mainly due to the nitrides formed during the nitriding process [40]. From the results obtained in this research work, the coatings that can be proposed for temporary implantation are Mg90–Zn10 and Mg85–Zn15 since they present more favorable corrosion and microhardness properties. In the same way, more studies on these coatings are planned to expand the findings from this work. Due to their properties, the prepared coatings can be applied as obturation or filler materials for bone deficiencies as a temporary implant. Surface modification by nitriding is an effective way to improve the corrosion resistance of magnesium alloys, in addition to contributing to surface bioactivity.

5. Conclusions

In this study, we investigated the mechanical properties, corrosion resistance, and cytotoxicity of Mg–Zn alloys and samples whose surface was modified by nitriding. Thus, the following conclusions can be drawn:

1. The alloys Mg95–Zn5, Mg90–Zn10, and Mg85–Zn15 (% by weight) were synthesized from Mg and Zn powders by MA, and the surfaces of the synthesized alloys were successfully modified by ion nitriding, improving their mechanical properties and corrosion resistance.
2. The XRD patterns showed the formation of a Mg–Zn intermetallic phase via the MA process. XRD detection showed that there were no impurities present in the synthesized samples in support of their application as biomaterials.
3. Potentiodynamic polarization curves displayed that pure Mg had lower corrosion resistance and a higher corrosion rate than the Mg–Zn alloys and nitrided samples, demonstrating that the Zn content and nitrides formed on the analyzed specimens can benefit from a protective layer on the surface of specimens, thereby increasing corrosion resistance and decreasing the corrosion rate in Hank's solution.
4. The results of cell viability tests, i.e., MTT assays, showed that extracts of Mg95–Zn5, Mg90–Zn10, and Mg85–Zn15 alloys and nitrided samples did not induce cytotoxicity towards fibroblast cells. Therefore, nitriding treatment may be a promising technique for improving the corrosion resistance and biocompatibility of Mg–Zn alloys for use as bone implants.

Author Contributions: Conceptualization, S.G. and A.M.; methodology, S.G., A.M., H.M. and E.L.-D.; formal analysis S.G., A.M., H.M. and E.V.-V.; Investigation, S.G., R.G., A.M. and H.M.; writing—original draft preparation, S.G., A.M. and E.L.-D.; writing—review and editing, E.V.-V. and H.M.; supervision, A.M.; Funding acquisition A.M. All authors have read and agreed to the published version of the manuscript.

Funding: This work was sponsored by CONAHCyT (beca Posdoctoral).

Data Availability Statement: The raw data supporting the conclusions of this article will be made available by the authors on request.

Conflicts of Interest: The authors declare no conflicts of interest.

References

1. Wu, S.; Liu, X.; Yeung, K.W.K.; Liu, C.; Yang, X. Biomimetic porous scaffolds for bone tissue engineering. *Mater. Sci. Eng. R Rep.* **2014**, *80*, 1–36. [[CrossRef](#)]
2. Han, H.-S.; Loffredo, S.; Jun, I.; Edwards, J.; Kim, Y.-C.; Seok, H.-K.; Witte, F.; Mantovani, D.; Glyn-Jones, S. Current status and outlook on the clinical translation of biodegradable metals. *Mater. Today* **2019**, *23*, 57–71. [[CrossRef](#)]
3. Hermawan, H. Updates on the research and development of absorbable metals for biomedical applications. *Prog. Biomater.* **2018**, *7*, 93–110. [[CrossRef](#)] [[PubMed](#)]
4. Kumar, A.; Pandey, P.M. Development of Mg based biomaterial with improved mechanical and degradation prop-erties using powder metallurgy. *J. Magnes. Alloy.* **2020**, *8*, 883–898. [[CrossRef](#)]
5. Xing, F.; Li, S.; Yin, D.; Xie, J.; Rommens, P.M.; Xiang, Z.; Liu, M.; Ritz, U. Recent progress in Mg-based alloys as a novel bioabsorbable biomaterials for orthopedic applications. *J. Magnes. Alloy.* **2022**, *10*, 1428–1456. [[CrossRef](#)]

6. Liu, Y.; Zheng, Y.; Chen, X.; Yang, J.; Pan, H.; Chen, D.; Wang, L.; Zhang, J.; Zhu, D.; Wu, S.; et al. Fundamental theory of biodegradable Metals—Definition, Criteria, and Design. *Adv. Funct. Mater.* **2019**, *29*, 1805402. [[CrossRef](#)]
7. Amaravathy, P.; Sowndarya, S.; Sathyanarayanan, S.; Rajendran, N. Novel sol gel coating of Nb₂O₅ on magnesium alloy for biomedical applications. *Surf. Coat. Technol.* **2014**, *244*, 131–141. [[CrossRef](#)]
8. Kekule, T.; Smola, B.; Vlach, M.; Kudrnova, H.; Kodetova, V.; Stulikova, I. Thermal stability and microstructure development of cast and powder metallurgy produced Mg–Y–Zn alloy during Heat treatment. *J. Magnes. Alloy.* **2017**, *5*, 173–180. [[CrossRef](#)]
9. Rodzi, S.N.H.M.; Zuhailawati, H.; Dhindaw, B. Mechanical and degradation behaviour of biodegradable magnesium–zinc/hydroxyapatite composite with different powder mixing techniques. *J. Magnes. Alloy.* **2019**, *7*, 566–576. [[CrossRef](#)]
10. Li, L.-Y.; Cui, L.-Y.; Zeng, R.-C.; Li, S.-Q.; Chen, X.-B.; Zheng, Y.; Kannan, M.B. Advances in functionalized polymer coatings on biodegradable magnesium alloys—A review. *Acta Biomater.* **2018**, *79*, 23–36. [[CrossRef](#)]
11. Al-Tamimi, A.A.; Fernandes, P.R.A.; Peach, C.; Cooper, G.; Diver, C.; Bartolo, P.J. Metallic bone fixation implants: A novel design approach for reducing the stress shielding phenomenon. *Virtual Phys. Prototyp.* **2017**, *12*, 141–151. [[CrossRef](#)]
12. Micheletti, C.; Lee, B.E.; Deering, J.; Binkley, D.M.; Coulson, S.; Hussanain, A.; Zurob, H.; Grandfield, K. Ti–5Al–5Mo–5V–3Cr bone implants with dual-scale topography: A promising alternative to ti–6al–4v. *Nanotechnology* **2020**, *31*, 235101. [[CrossRef](#)] [[PubMed](#)]
13. Sezer, N.; Evis, Z.; Kayhan, S.M.; Tahmasebifar, A.; Koç, M. Review of magnesium-based biomaterials and their applications. *J. Magnes. Alloy.* **2018**, *6*, 23–43. [[CrossRef](#)]
14. Riaz, U.; Shabib, I.; Haider, W. The current trends of Mg Alloys in biomedical applications—A review. *J. Bio-Med. Mater. Res. Part B Appl. Biomater.* **2018**, *107*, 1970–1996. [[CrossRef](#)] [[PubMed](#)]
15. Song, M.-S.; Zeng, R.-C.; Ding, Y.-F.; Li, R.W.; Easton, M.; Cole, I.; Birbilis, N.; Chen, X.-B. Recent advances in bio-degradation controls over Mg alloys for bone fracture management: A review. *J. Mater. Sci. Technol.* **2019**, *35*, 535–544. [[CrossRef](#)]
16. Shahin, M.; Munir, K.; Wen, C.; Li, Y. Magnesium matrix nanocomposites for orthopedic applications: A review from mechanical, corrosion, and biological perspectives. *Acta Biomater.* **2019**, *96*, 1–19. [[CrossRef](#)] [[PubMed](#)]
17. Yang, J.; Koons, G.L.; Cheng, G.; Zhao, L.; Mikos, A.G.; Cui, F.-Z. A review on the exploitation of biodegradable magnesium-based composites for medical applications. *Biomed. Mater.* **2018**, *13*, 022001. [[CrossRef](#)]
18. Amukarimi, S.; Mozafari, M. Biodegradable Magnesium Biomaterials—Road to the Clinic. *Bioengineering* **2022**, *9*, 107. [[CrossRef](#)]
19. Lesz, S.; Karolus, M.; Gabryś, A.; Kremzer, M. Influence of Milling Time on Phase Composition and Product Structure of Mg–Zn–Ca–Ag Alloys Obtained by Mechanical Synthesis. *Materials* **2022**, *15*, 7333. [[CrossRef](#)]
20. Habraken, W.; Habibovic, P.; Epple, M.; Bohner, M. Calcium phosphates in biomedical applications: Materials for the future? *Mater. Today* **2016**, *19*, 69–87. [[CrossRef](#)]
21. Kravanja, K.A.; Finšgar, M. A review of techniques for the application of bioactive coatings on metal-based implants to achieve controlled release of active ingredients. *Mater. Des.* **2022**, *217*, 110653. [[CrossRef](#)]
22. Razavi, M.; Fathi, M.; Savabi, O.; Razavi, S.M.; Beni, B.H.; Vashae, D.; Tayebi, L. Controlling the degradation rate of bioactive magnesium implants by electrophoretic deposition of akermanite coating. *Ceram. Int.* **2014**, *40*, 3865–3872. [[CrossRef](#)]
23. Omar, S.; Ballarre, J.; Castro, Y.; Campos, E.M.; Schreiner, W.; Durán, A.; Cere, S. 58S and 68S sol-gel glass-like bioactive coatings for enhancing the implant performance of AZ91D magnesium alloy. *Surf. Coat. Technol.* **2020**, *400*, 126224. [[CrossRef](#)]
24. Gnedenkov, A.; Sinebryukhov, S.; Filonina, V.; Gnedenkov, S. Hydroxyapatite-containing PEO-coating design for biodegradable Mg–0.8Ca alloy: Formation and corrosion behaviour. *J. Magnes. Alloy.* **2022**, *11*, 4468–4484. [[CrossRef](#)]
25. Sedelnikova, M.; Ivanov, K.; Ugodchikova, A.; Kashin, A.; Uvarkin, P.; Sharkeev, Y.; Tolkacheva, T.; Tolmachev, A.; Schmidt, J.; Egorin, V.; et al. The effect of pulsed electron irradiation on the structure, phase composition, adhesion and corrosion properties of calcium phosphate coating on Mg0.8Ca alloy. *Mater. Chem. Phys.* **2023**, *294*, 126996. [[CrossRef](#)]
26. Farshid, S.; Kharaziha, M.; Atapour, M. A self-healing and bioactive coating based on duplex plasma electrolytic oxidation/polydopamine on AZ91 alloy for bone implants. *J. Magnes. Alloy.* **2023**, *11*, 592–606. [[CrossRef](#)]
27. Gnedenkov, A.; Sinebryukhov, S.; Filonina, V.; Plekhova, N.; Gnedenkov, S. Smart composite antibacterial coatings with active corrosion protection of magnesium alloys. *J. Magnes. Alloy.* **2022**, *10*, 3589–3611. [[CrossRef](#)]
28. Bagale, U.D.; Desale, R.; Sonawane, S.H.; Kulkarni, R.D. An Active Corrosion Inhibition Coating of Two Pack Epoxy Polyamide System using Halloysite Nanocontainer. *Prot. Met. Phys. Chem. Surf.* **2018**, *54*, 230–239. [[CrossRef](#)]
29. Wang, Y.; Yang, Y.; Yang, H.; Zhang, M.; Ma, S.; Qiao, J. Microstructure and wear properties of nitrided AlCoCrFeNi high-entropy alloy. *Mater. Chem. Phys.* **2018**, *210*, 233–239. [[CrossRef](#)]
30. Duong Nam, N.; Anh Xuan, N.; Van Bach, N.; Nhung, L.T.; Chieu, L.T. Control gas nitriding process: A review. *J. Mech. Eng. Res. Dev.* **2019**, *42*, 17–25. [[CrossRef](#)]
31. Ganda, A.N.; Wijaya, H.; Dewi, F.G. Influence of surface roughness on corrosion behaviour of 316L stainless steel in artificial saliva and body fluid. *IOP Conf. Ser. Mater. Sci. Eng.* **2021**, *1034*, 012158. [[CrossRef](#)]
32. Fischer, D.A.; Vargas, I.T.; Pizarro, G.E.; Armijo, F.; Walczak, M. The effect of scan rate on the precision of determining corrosion current by Tafel extrapolation: A numerical study on the example of pure Cu in chloride containing medium. *Electrochim. Acta* **2019**, *313*, 457–467. [[CrossRef](#)]
33. ISO 10993–12 2012; Biological Evaluation of Medical Devices, Part 12: Sample Preparation and Reference Materials. ISO: Geneva, Switzerland, 2012.

34. Wyckoff, R.W.G. Hexagonal closest packed, hcp, structure. In *Crystal Structures*, 2nd ed.; Interscience Publishers: New York, NY, USA, 1963; Volume 1, pp. 7–83.
35. Yan, Y.; Chu, X.; Luo, X.; Xu, X.; Zhang, Y.; Dai, Y.; Li, D.; Chen, L.; Xiao, T.; Yu, K. A homogenous microstructural Mg-based matrix model for orthopedic application with generating uniform and smooth corrosion product layer in Ringer's solution: Study on biodegradable behavior of Mg-Zn alloys prepared by powder metallurgy as a case. *J. Magnes. Alloy.* **2020**, *9*, 225–240. [[CrossRef](#)]
36. Salleh, E.M.; Zuhailawati, H.; Ramakrishnan, S. Synthesis of biodegradable Mg-Zn alloy by mechanical alloying: Statistical prediction of elastic modulus and mass loss using fractional factorial design. *Trans. Nonferrous Met. Soc. China* **2018**, *28*, 687–699. [[CrossRef](#)]
37. Rajabi, M.; Sedighi, R.; Rabiee, S. Thermal stability of nanocrystalline Mg-based alloys prepared via mechanical alloying. *Trans. Nonferrous Met. Soc. China* **2016**, *26*, 398–405. [[CrossRef](#)]
38. Kapinos, D.; Augustyn, B.; Szymanek, M. Methods of introducing alloying elements into liquid magnesium. *Metall. Foundry Eng.* **2014**, *40*, 141. [[CrossRef](#)]
39. Pokharel, D.B.; Wu, L.; Dong, J.; Yadav, A.P.; Subedi, D.B.; Dhakal, M.; Zha, L.; Mu, X.; Umoh, A.J.; Ke, W. Effect of glycine addition on the in-vitro corrosion behavior of AZ31 magnesium alloy in Hank's solution. *J. Mater. Sci. Technol.* **2021**, *81*, 97–107. [[CrossRef](#)]
40. Yan, F.; Chen, B.; Yao, J.; Zhang, D.; Yan, M.; Zhang, Y. Characterization of microstructure and corrosion properties of AZ91D magnesium alloy surface-treated by coating-nitriding. *J. Mater. Res. Technol.* **2021**, *14*, 1559–1568. [[CrossRef](#)]
41. Koç, E.; Kannan, M.B.; Ünal, M.; Candan, E. Influence of zinc on the microstructure, mechanical properties and in vitro corrosion behavior of magnesium–zinc binary alloys. *J. Alloys Compd.* **2015**, *648*, 291–296. [[CrossRef](#)]
42. Zhong, Q.; Pan, D.; Zuo, S.; Li, X.; Luo, H.; Lin, Y. Fabrication of MgZn intermetallic layer with high hardness and corrosion resistance on az31 alloy. *Mater. Charact.* **2021**, *179*, 111365. [[CrossRef](#)]
43. Sun, Y.; Helmholz, H.; Willumeit-Römer, R. Preclinical in vivo research of magnesium-based implants for fracture treatment: A systematic review of animal model selection and study design. *J. Magnes. Alloy.* **2020**, *9*, 351–361. [[CrossRef](#)]
44. Kose, O.; Turan, A.; Unal, M.; Acar, B.; Guler, F. Fixation of medial malleolar fractures with magnesium bioabsorbable headless compression screws: Short-term clinical and radiological outcomes in eleven patients. *Arch. Orthop. Trauma Surg.* **2018**, *138*, 1069–1075. [[CrossRef](#)] [[PubMed](#)]
45. Wang, J.; Xu, J.; Hopkins, C.; Chow, D.H.; Qin, L. Biodegradable Magnesium-Based Implants in Orthopedics—A General Review and Perspectives. *Adv. Sci.* **2020**, *7*, 1902443. [[CrossRef](#)]
46. Zhao, M.-C.; Zhao, Y.-C.; Yin, D.-F.; Wang, S.; Shangguan, Y.-M.; Liu, C.; Tan, L.-L.; Shuai, C.-J.; Yang, K.; Atrens, A. Biodegradation Behavior of Coated As-Extruded Mg–Sr Alloy in Simulated Body Fluid. *Acta Met. Sin.* **2019**, *32*, 1195–1206. [[CrossRef](#)]
47. Palcut, M.; Kaľavská, M.; Ďuriška, L.; Černičková, I.; Adamech, M.; Janovec, J. Corrosion behavior of Zn-Mg and Zn-Mg-Y alloys. *AIP Conf. Proc.* **2023**, *2778*, 040021.
48. Zhang, S.; Zhang, X.; Zhao, C.; Li, J.; Song, Y.; Xie, C.; Tao, H.; Zhang, Y.; He, Y.; Jiang, Y.; et al. Research on an Mg–Zn alloy as a degradable biomaterial. *Acta Biomater.* **2010**, *6*, 626–640. [[CrossRef](#)]

Disclaimer/Publisher's Note: The statements, opinions and data contained in all publications are solely those of the individual author(s) and contributor(s) and not of MDPI and/or the editor(s). MDPI and/or the editor(s) disclaim responsibility for any injury to people or property resulting from any ideas, methods, instructions or products referred to in the content.